

# Temperature Cycling Enables Efficient $^{13}\text{C}$ SABRE-SHEATH Hyperpolarization and Imaging of $[1-^{13}\text{C}]$ Pyruvate

Patrick TomHon\*, Mustapha Abdulmojeed, Isaiah Adelabu, Shiraz Nantogma, Mohammad Shah Hafez Kabir, Sören Lehmkuhl, Eduard Y. Chekmenev, and Thomas Theis\*

**ABSTRACT:** Current metabolic imaging in humans is dominated by positron emission tomography (PET) methods. An emerging non-ionizing alternative for molecular imaging is hyperpolarized MRI. In particular, imaging of hyperpolarized  $^{13}\text{C}$ -pyruvate is a leading candidate because pyruvate is innocuous and has a central role in metabolism. However, similar to PET, hyperpolarized MRI with dynamic nuclear polarization (DNP) is complex, costly and requires complex infrastructure. In contrast, signal amplification by reversible exchange (SABRE) is a fast, cheap, and scalable hyperpolarization technique. In particular, SABRE in SHield Enables Alignment Transfer to Heteronuclei (SABRE-SHEATH) transfers polarization from parahydrogen to  $^{13}\text{C}$  in pyruvate, however, to date, SABRE-SHEATH of  $^{13}\text{C}$ -pyruvate was limited in polarization levels relative to DNP (1.7% with SABRE-SHEATH vs. ~60% with DNP). Here we introduce a temperature cycling method for SABRE-SHEATH that enables >10% polarization on  $[1-^{13}\text{C}]$ pyruvate, sufficient for successful *in vivo* experiments. First, at lower temperatures, ~20% polarization is accumulated on SABRE-catalyst bound pyruvate, which is subsequently released into free pyruvate in solution at elevated temperatures. We take advantage of the achieved polarization to demonstrate first  $^{13}\text{C}$  pyruvate images with a cryogen-free MRI system operated at 1 T. This illustrates that inexpensive hyperpolarization methods can be combined with low-cost MRI systems to obtain a broadly available, yet highly sensitive metabolic imaging platform.

Current metabolic imaging is dominated by PET and SPECT, which require synchrotrons and radiochemistry to produce radioactive injectables. In contrast, hyperpolarized MRI is emerging as a technique that enables tracking of biomolecular metabolism without radioactive labels and ionizing radiation.<sup>1</sup> Hyperpolarized (HP) MRI can be used to gain insights and diagnose metabolic disease states such as cancer<sup>1</sup>, diabetes<sup>2</sup>, and cardiovascular disease<sup>3,4</sup>. HP pyruvate has emerged as a leading candidate as metabolic marker due to its safety and its central role in metabolism.<sup>1</sup> For example, pyruvate to lactate conversion is upregulated in cancer cells, enabling early detection of cancer cells.<sup>1,5,6</sup> Striking advancements have been made in applications to prostate<sup>5,7</sup>, breast<sup>8</sup>, and brain<sup>9</sup> tissues<sup>10</sup>. However, the leading method to hyperpolarize pyruvate, dissolution dynamic nuclear polarization (d-DNP), is limited in broad availability due to its high cost (~\$2.5M), long contrast agent production times (~30 min or more), and instrument complexity.<sup>11,12</sup> Specifically, d-DNP transfers electron polarization to nuclei using high power microwaves at cryogenic temperatures of ~1 K inside superconducting magnets, and this process is followed by rapid dissolution with a superheated solvent.<sup>11,13</sup> In contrast, Signal Amplification By Reversible Exchange (SABRE) is a fast (~20 s), cheap (~\$25k), and scalable hyperpolarization technique using parahydrogen ( $p\text{-H}_2$ ) as a source of spin order. SABRE hyperpolarizes small molecules in solutions that could readily be used for metabolic imaging of many compounds including pyruvate.<sup>14-17</sup>

SABRE in its original implementation was optimized to hyperpolarized protons at mT magnetic fields<sup>14</sup>, whereas the hyperpolarization of heteronuclei, including  $^{15}\text{N}$  and  $^{13}\text{C}$ , is optimized in magnetic shields that establish  $\mu\text{T}$  magnetic

fields. This approach is called SABRE in SHield Enables Alignment Transfer to Heteronuclei (SABRE-SHEATH).<sup>18-20</sup> Previous work has demonstrated the feasibility of  $^{13}\text{C}$  pyruvate hyperpolarization with SABRE-SHEATH, but remained limited in polarization relative to the high values of DNP (1.7% vs. ~60%).<sup>15,16</sup> Here, we present a combination of advances including the use of temperature cycling to overcome the *in vivo* polarization threshold of 10% with SABRE-SHEATH. The results of this study also indicate that further optimization of  $[1-^{13}\text{C}]$ pyruvate SABRE-SHEATH is possible to maximize the critical molar polarization, defined as the product of concentration and polarization (introduced by Knecht et al.<sup>21</sup>), which is ultimately the most important hyperpolarization parameter required for *in vivo* translation.<sup>7,12,22</sup>

Previous demonstrations of parahydrogen induced polarization (PHIP) on pyruvate have shown the feasibility of *in vivo* studies. Specifically, these experiments have shown that 10% initial polarization with a 35 mM pyruvate injection is sufficient for hyperpolarized *in vivo* MRI<sup>23</sup>, a threshold that we reach using the SABRE-SHEATH technique in this study. These early demonstrations relied on the direct incorporation of  $p\text{-H}_2$  into an unsaturated precursor through hydrogenation to obtain the target molecule such as fumarate.<sup>24-26</sup> Similarly, HP pyruvate can be obtained from the addition of  $p\text{-H}_2$  to propargyl pyruvate followed by rapid hydrolysis of vinyl pyruvate to pyruvate.<sup>23,27</sup> This process was called PHIP by side-arm hydrogenation (PHIP-SAH) but involves synthesis of the propargyl pyruvate precursor, hydrogenation, complex spin transfer, hydrolysis, and phase transfer steps to obtain HP pyruvate.<sup>23</sup> In contrast, the facile nature of SABRE enables

direct hyperpolarization of the  $^{13}\text{C}$  spins in pyruvate, accessing rapid polarization without additional complex steps.

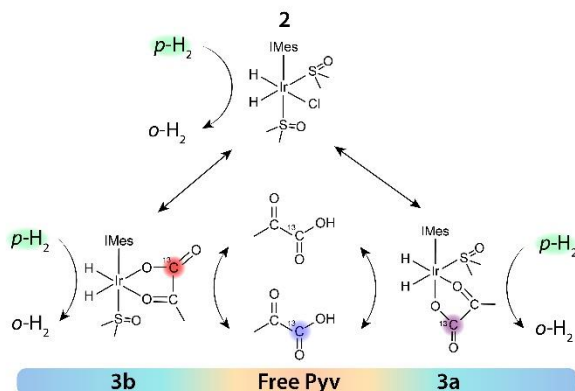


**Figure 1.** Hyperpolarization scheme of  $[1-^{13}\text{C}]$ pyruvate, with a gradient representation of temperature cycling. The full IMes ligand is omitted for diagram clarity, where IMes = 1,3 - bis(2,4,6 - trimethylphenyl) imidazole-2-ylidene.

Rapid polarization of  $[1-^{13}\text{C}]$ pyruvate using SABRE-SHEATH is achieved in this study using DMSO as a co-ligand, accessing a reaction network illustrated in Figure 1. This figure highlights the different active catalytic species originally described by Tickner et al., where optimized hyperpolarization levels of  $[1,2-^{13}\text{C}_2]$ pyruvate reached 1.7%,<sup>16</sup> which remained below the 6.2% (~10% nascent) polarization achieved with the PHIP-SAH approach.<sup>23,28</sup> In the present work, we highlight that sufficiently fast  $p\text{-H}_2$  exchange still occurs in the complex at low temperatures. We take advantage of this feature and implement temperature gradients with SABRE-SHEATH on  $[1-^{13}\text{C}]$ pyruvate to reach  $P_{^{13}\text{C}}$  ( $^{13}\text{C}$  polarization) ~10.8% on free pyruvate in solution, over six times greater than previous optimized results (Figure 2A). This is enabled by starting with

$P_{^{13}\text{C}}$  ~20 % on catalyst bound pyruvate at lower temperatures. We provide detailed insights regarding exchange dynamics and relaxation processes during temperature gradients, which modulate substrate and hydride exchange rates. The initial results of this study also indicate that further optimization of the pyruvate SABRE-SHEATH process can yield higher molar polarization levels (concentration  $\times$  %P) as needed for *in vivo* studies.<sup>10,21,23</sup>

The spectrum and results shown in figure 2A are the maximum achieved single-shot polarization during this study. This data shows 14.3% polarization on the bound pyruvate species, and 10.8% on the free pyruvate corresponding to a total sample polarization of 11.8% on pyruvate. Full details of the polarization calculations are given in the SI whereas detailed characterization of the dynamics are provided at the end of this manuscript. The central hallmarks that allowed the reported polarization levels are:

- 1) Use of  $[1-^{13}\text{C}]$ pyruvate. Both  $[2-^{13}\text{C}]$ pyruvate and  $[1,2-^{13}\text{C}_2]$ pyruvate polarization levels remain below those found for  $[1-^{13}\text{C}]$ pyruvate (See SI).
- 2) Use of high catalyst to substrate ratio (5 eqv. pyruvate, 3.3 eqv. DMSO), as reported in previous work.<sup>16,29</sup>
- 3) Pre-cooling the sample to slow exchange (as indicated in Figure 1) followed by bubbling at elevated temperature causing a temperature gradient over the course of the build-up time.

Using the high polarization achieved on  $[1-^{13}\text{C}]$ pyruvate, we also acquired a  $^{13}\text{C}$  image using a fast spin echo sequence at 1.0 T of a cryogen-free MRI system that can be operated at any field between 5 mT and 3 T. At the clinically relevant field of 1 T, we imaged the sample directly in an NMR tube with sub-mm resolution (Figure 2C). As shown in these images, the HP signal enables 3D multi-slice imaging of the 3.47 mm cross-sectional area of the NMR tube. The images are not optimized due to the rough

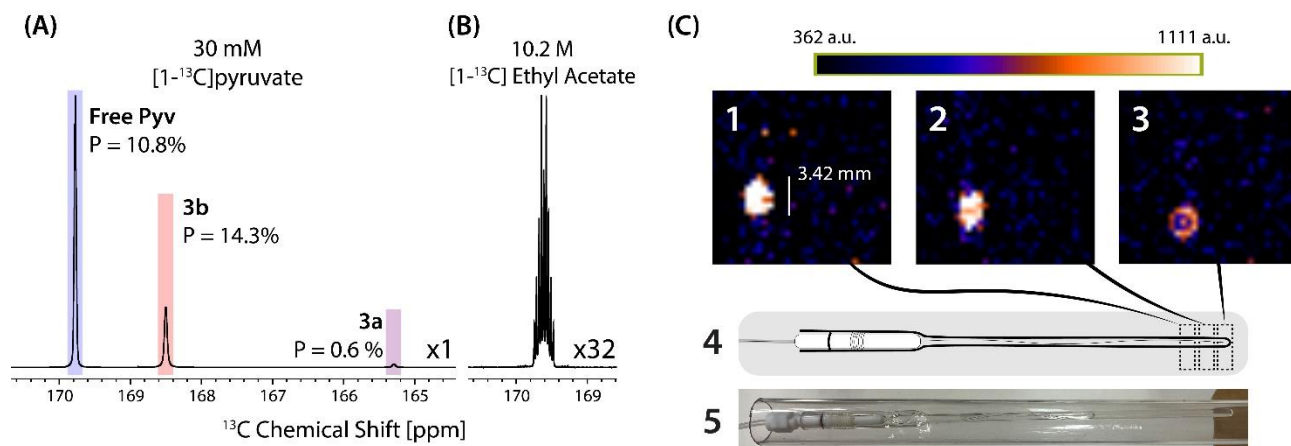


**Figure 2.** (A) NMR spectrum of hyperpolarized  $[1-^{13}\text{C}]$ pyruvate in free and catalyst bound forms. This spectrum was acquired with a sample of 30 mM  $[1-^{13}\text{C}]$ pyruvate, 20 mM DMSO, and 6 mM IMes catalyst. (B) Thermal reference spectrum of  $[1-^{13}\text{C}]$ ethyl acetate at 9.4 T, used for calculation of the polarization. (C) MRI of HP  $[1-^{13}\text{C}]$ pyruvate sample. Three slices of the image are taken in 1-3, with the NMR tube phantom and corresponding slice positioning shown in 4 and 5. The images are acquired with a fast spin echo sequence at 1.0 T with  $32 \times 32$  voxels,  $20 \times 20 \text{ mm}^2$  FOV, an echo train length of 16 lines, and an overall acquisition time of 3.3 s. Full details regarding the setup and sequence are in the SI.

positioning of the NMR tube in the coil volume giving variable shims when the NMR tube is inserted into the scanner. A corresponding spectrum of HP  $[1-^{13}\text{C}]$ pyruvate characterizing the inhomogeneities in the MRI is given in the SI.

The variable temperature control before and during  $p\text{-H}_2$  bubbling is crucial to maximize the observed polarization levels. First, exchange is slowed with a low initial temperature but increases as the sample is bubbled at the SABRE polarization transfer field (PTF) at an elevated temperature. For the experiments depicted in Figures 3A-E, we used a previously described pneumatic shuttling system,<sup>30</sup> where the sample is first cooled in the probe with a variable temperature unit and subsequently shuttled out of the cooled atmosphere into magnetic shields at approximately 18 °C and SABRE-SHEATH<sup>15,31,32</sup> matching field of 0.4  $\mu\text{T}$ . At a short bubbling time of 15 s, there is only a small deviation in the sample temperature of less than 4 °C. However, at a longer bubbling time (90 s) the samples experience larger rise in temperature of about 14 °C. To characterize the warming process, Figure 3E shows the change in sample temperature as a function of bubbling time when starting at a sample temperature of 0 °C. The temperature was assessed based on the NMR-frequency shift of the exchangeable methanol proton. The full details of these calibrations are explained in the SI.

At low initial temperature, the slower exchange promotes efficient polarization buildup on the catalyst-bound pyruvate. This effect is evidenced by up to 20% polarization on the catalyst-bound pyruvate achieved by starting at the lowest temperature of -10 °C (see Fig. 3C). With only 15 s of bubbling (Fig. 3B) the polarization remains almost exclusively on the bound species **3b**. We note that in contrast to previous work,<sup>16</sup> our data suggests that even at low temperatures, efficient hydrogen exchange still occurs on both the **3b** and **3a** catalytic species, whereas bound pyruvate barely exchanges.

As the sample warms during the bubbling period HP  $[1-^{13}\text{C}]$ pyruvate can exchange off the catalyst more rapidly while continued SABRE occurs as the sample warms, ultimately leading to high polarization on free pyruvate. As is evident from Fig. 3B and C, at even further elevated temperatures the free and bound polarization numbers equilibrate as expected with efficiently exchanging pools.

The maximum in free pyruvate polarization of 10.8% is observed with an initial temperature of 5 °C, which increases to 14 °C over 90 s bubbling (Figure 3C). A full investigation of the kinetics of these temperature cycling effects will be the subject of future work using either linewidth<sup>33,34</sup> or EXSY<sup>35</sup> analyses.

To unequivocally confirm that experiments with a temperature gradient give higher polarization than experiments with constant temperatures we conducted a study that allowed for fully comparable experiments with constant temperature established with a water bath. To perform such direct comparison, we had to switch to manual sample transfer experiments with a 1.1 T benchtop NMR spectrometer. The results are displayed in Figure 3F. The sample is either bubbled in a water bath at constant temperature in a magnetic shield (purple, Figure 3F) or first pre-cooled in a water bath at a set temperature and then bubbled in the shield at ambient temperature (green, Figure

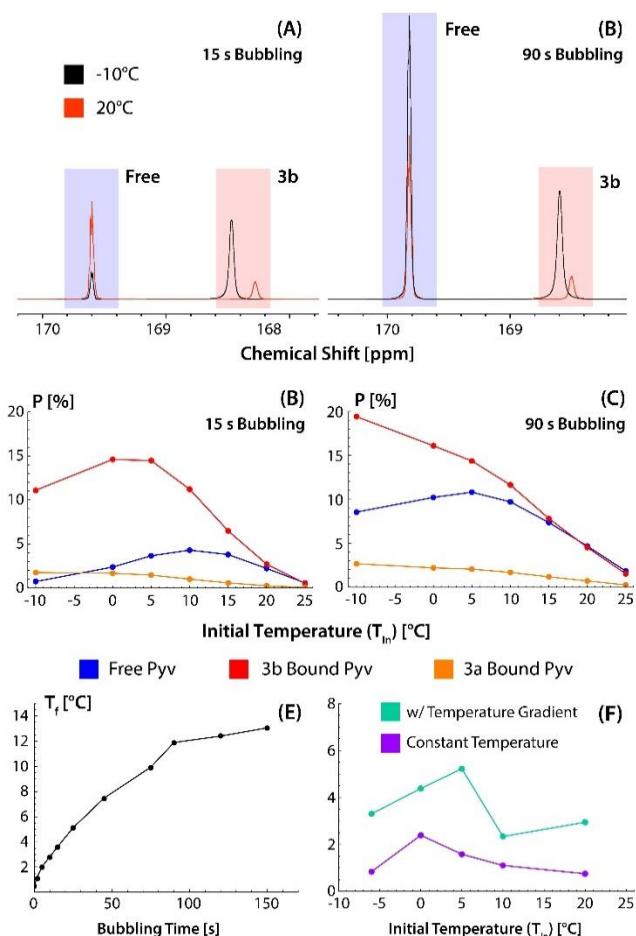


**Figure 3.** Variable temperature comparisons in the hyperpolarization of  $[1-^{13}\text{C}]$ pyruvate. (A,B) Comparison of HP spectra obtained with an initial sample temperature of -10°C and 20°C using (A) 15 s bubbling and (B) 90 s bubbling. (C,D) Comparison of the temperature dependence of  $[1-^{13}\text{C}]$ pyruvate hyperpolarization with (C) 15 s bubbling and (D) 90 s bubbling. (E) Final sample temperature with variable bubbling time for an initial sample temperature of 0°C in the pneumatic shuttling setup. (F) Comparison of polarization obtained on free pyruvate with and without a temperature gradient using manual sample transfer. All data was acquired with a 0.3  $\mu\text{T}$  PTF and 100 psi  $p\text{-H}_2$  at 75 sccm on a sample of 6 mM Ir-IMes catalyst, 20 mM DMSO and 30 mM  $[1-^{13}\text{C}]$ pyruvate.

3F). The constant temperature experiments consistently stay below the experiments with temperature gradients.

The lower relative polarization values in this data, compared to the data acquired with shuttling, are due to inconsistencies and lack of reproducibility in manually moving the sample. Manual sample transfer takes longer than automated shuttling and full adiabaticity could not be guaranteed. Nonetheless, the experiments with a temperature gradient consistently give higher polarization than experiments at constant temperature.

Figure 4 details dependence on magnetic field (4A), build-up time (4B) and  $T_1$  relaxation delays (4C,D),  $p\text{-H}_2$  pressure (4E), and pyruvate concentration (4F). In Fig. 4A, we observe a standard PTF dependence for SABRE-

SHEATH<sup>32</sup>, with typical maxima observed at  $\sim 0.3$  to  $0.4 \mu\text{T}$ . Figure 4B shows that the polarization buildup is fast relative to the  $0.3 \mu\text{T}$  relaxation rate displayed in Figure 4D. In the build-up curves of Figure 4B the pronounced differences between free and bound pyruvate polarization buildup stem from the temperature gradient. At lower temperatures early in the buildup, the bound species polarizes quickly and efficiently. As faster exchange is induced at longer bubbling times during sample warming, the polarization is transferred to the free pyruvate, which accordingly displays a slower buildup rate. Based on the observed behavior, it is expected that the build-up rates will depend on the chosen temperature gradient.

The exchange between free and bound pyruvate also plays an important role in the acquired relaxation data shown in Fig. 4C and D. In Fig. 4C polarization is measured as a function of a variable delay at 9.4 T. These experiments are conducted by first bubbling for 90 s at the  $\mu\text{T}$ -PTF, raising the sample temperature to  $\sim 12^\circ\text{C}$ . Then the sample is shuttled back to the bore of the magnet, where the sample gradually cools back down to the initial temperature of  $0^\circ\text{C}$ . The data in Figure 4C does not fit a single exponential because two effects play out at the same time: a) relaxation and b) the equilibration of polarization of free and bound pyruvate as promoted by exchange.

Immediately after arriving at high field, the polarization of the bound pyruvate is  $\sim 15\%$ , which is larger than the polarization of the free pyruvate of  $\sim 10\%$ . At short delay times, the highly polarized bound pyruvate continues to exchange into the free pyruvate pool, raising the free polarization of the free pyruvate. In contrast, the bound pyruvate polarization initially decreases at a faster rate because of the combined effect of relaxation and the exchange with the less polarized free pool. As the polarization of the pools equilibrates with increasing delays, and

the sample temperature drops suppressing exchange, the relaxation behavior exhibits typical mono-exponential character for both free and bound pyruvate.

An analogous effect can be observed in the measurement of low-field (LF,  $0.3 \mu\text{T}$ ) relaxation times displayed in Figure 4D. At short time delays at LF the free polarization continues to increase initially, as the two polarization pools are in exchange and the bound pool transfers its polarization into the free pool. However, in contrast to the 9.4 T experiments, at  $0.3 \mu\text{T}$  exchange increases with the variable delay time as the sample is held at the elevated ambient temperature. The result is that the bound and free pools mix more efficiently at long delay times and decay at similar rates after the equilibration of the polarization pools is complete.

Figure 4E shows an important effect that  $p\text{-H}_2$  is not the limiting substrate at pressures above  $\sim 75$  psi for the investigated sample composition of 6 mM Ir-IMes catalyst, 20 mM DMSO and 30 mM  $[1\text{-}^{13}\text{C}]\text{pyruvate}$ . This graph implies that at higher substrate and catalyst concentrations the parahydrogen pressure can be increased to maintain the same polarization levels while boosting the ultimately important molar polarization.

This insight is further stressed by the results displayed in Fig. 4F, which demonstrate the scalability of  $^{13}\text{C}$  pyruvate polarization from 30 mM  $[1\text{-}^{13}\text{C}]\text{pyruvate}$  (where all the previously discussed results were obtained) to 60 mM  $[1\text{-}^{13}\text{C}]\text{pyruvate}$  (maintaining the same ratios of catalyst and DMSO). First, doubling of the concentration leads to an increase in polarization, therefore more than doubling the molar polarization. Shifting to an even higher concentration near the maximum solubility of sodium pyruvate in methanol (75 mM) yielded a reduced polarization, however still increased the molar polarization. We believe, that the 60 mM pyruvate sample may be ideal for future studies and *in vivo* investigations. Furthermore, these

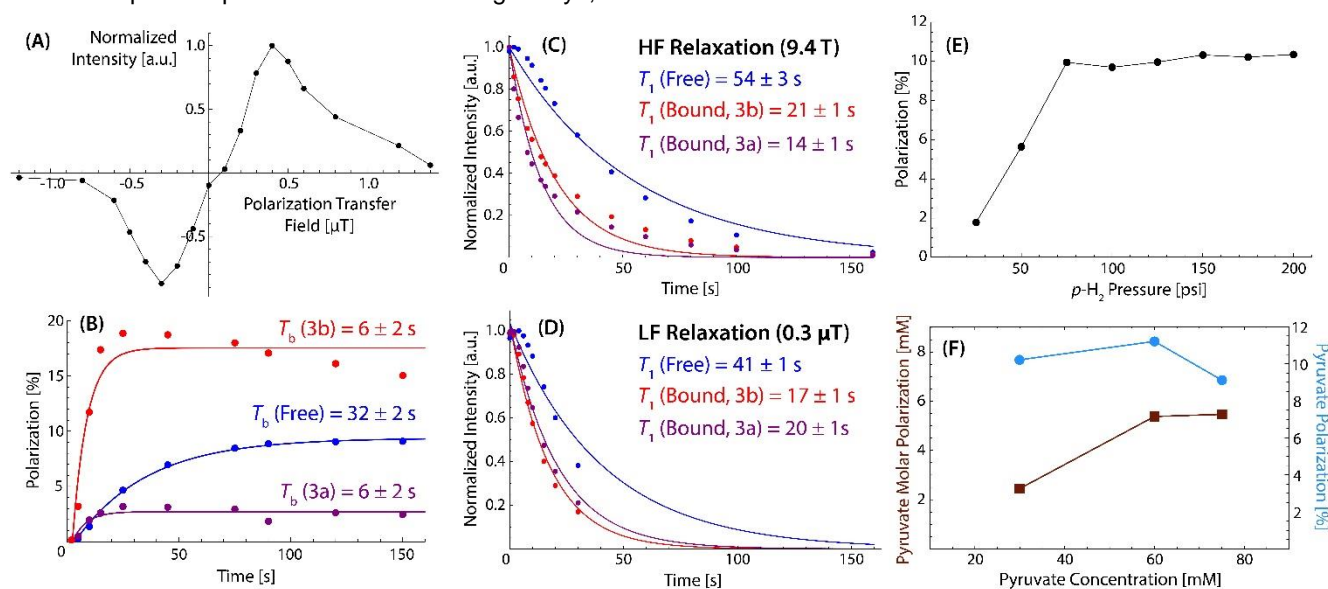


**Figure 4.** Measurement of  $^{13}\text{C}$  hyperpolarization as a function of (A) polarization transfer field, (B) polarization buildup time, (C)  $T_1$  relaxation delay at 9.4 T, (D)  $T_1$  relaxation delay at  $0.3 \mu\text{T}$ , (E)  $p\text{-H}_2$  pressure, and (F) sample concentration. Catalyst and DMSO concentrations are scaled together with the pyruvate concentration in (F) maintaining the same ratios. Unless varied, all data is acquired with a  $0.3 \mu\text{T}$  PTF and 100 psi  $p\text{-H}_2$  at 75 sccm on 6 mM Ir-IMes catalyst, 20 mM DMSO and 30 mM  $[1\text{-}^{13}\text{C}]\text{pyruvate}$ .

higher concentrated samples are likely to be parahydrogen limited (see Fig. 4E) and higher  $p\text{-H}_2$  pressures may return the same polarization levels while boosting molar polarization.

In conclusion, we demonstrated a high (11.8% weighted average) total polarization for  $[1\text{-}^{13}\text{C}]$ pyruvate and 10.8% free polarization paving the way for further optimization and significantly enhancing the feasibility of *in vivo* work. Specifically, the facile and robust nature of SABRE hyperpolarization relative to other hyperpolarization methods make it an easily scalable technology. In these results we also emphasize the important role the choice of spin system, sample composition, and temperature gradients play in achieving high polarization levels. We used the high polarization levels to acquire multi-slice HP  $^{13}\text{C}$  images with a cryogen-free MRI system operated at 1 T. This achievement indicates that it is possible to combine low-cost hyperpolarization with low-cost MRI to achieve high-sensitivity molecular imaging. Future work will focus on partnering these methods with previous demonstrations of catalyst extraction<sup>36</sup> or phase-switching<sup>37</sup> to achieve safely injectable solutions for *in vivo* demonstrations at the preclinical level, ultimately driving this technology from discovery to application.

## AUTHOR INFORMATION

### Corresponding Authors

\* Patrick TomHon – Department of Chemistry, North Carolina State University, Raleigh, North Carolina 27695, United States

\* Thomas Theis – Department of Chemistry, North Carolina State University, Raleigh, North Carolina 27695, United States; Joint Department of Biomedical Engineering, University of North Carolina, Chapel Hill and North Carolina State University, Raleigh, North Carolina 27606, United States; Department of Physics, North Carolina State University, Raleigh, North Carolina 27695, United States

### Authors

Mustapha Abdulmojeed – Department of Chemistry, North Carolina State University, Raleigh, North Carolina 27695, United States

Isaiah Adelabu – Department of Chemistry, Wayne State University, Detroit, Michigan 48202, United States

Shiraz Nantogma – Department of Chemistry, Wayne State University, Detroit, Michigan 48202, United States

Mohammad Shah Hafez Kabir – Department of Chemistry, Wayne State University, Detroit, Michigan 48202, United States

Sören Lehmkuhl – Department of Chemistry, North Carolina State University, Raleigh, North Carolina 27695, United States

Eduard Y. Chekmenev – Department of Chemistry, Wayne State University, Detroit, Michigan 48202, United States; Integrative Biosciences (Ibio), Wayne State University, Detroit, MI, 48202, United States; Karmanos Cancer Institute (KCI), Wayne State University, Detroit, MI, 48202, United States; Russian Academy of Sciences, Leninsky Prospekt 14, 119991 Moscow, Russia

### Notes

Thomas Theis holds stock in Vizma Life Sciences LLC (VLS) and is President of VLS. VLS is developing products

related to the research being reported. The terms of this arrangement have been reviewed and approved by NC State University in accordance with its policy on objectivity in research. The authors have filed a provisional patent application through NC State University with the USPTO regarding this work. EYC discloses a stake of ownership in XeUS Technologies, LTD.

## ACKNOWLEDGMENT

Research reported in this publication was supported by the National Institute of Biomedical Imaging and Bioengineering of the National Institutes of Health under Award Numbers NIH R21-EB025313 and NIH R01EB029829. The content is solely the responsibility of the authors and does not necessarily represent the official views of the National Institutes of Health. In addition, we acknowledge funding from the Mallinckrodt Foundation, the National Science Foundation under award NSF CHE-1904780, and from the National Cancer Institute under award number NCI 1R21CA220137, as well as funding from the North Carolina Biotechnology Center in the form of a Translational Research Grant.

## REFERENCES

- (1) Serrao, E. M.; Brindle, K. M. Potential Clinical Roles for Metabolic Imaging with Hyperpolarized  $[1\text{-}^{13}\text{C}]$ Pyruvate. *Front. Oncol.* **2016**, 6 (MAR), 1–6.
- (2) Rider, O. J.; Apps, A.; Miller, J. J. J.; Lau, J. Y. C.; Lewis, A. J. M.; Peterzan, M. A.; Dodd, M. S.; Lau, A. Z.; Trumper, C.; Gallagher, F. A.; Grist, J. T.; Brindle, K. M.; Neubauer, S.; Tyler, D. J. Noninvasive *In Vivo* Assessment of Cardiac Metabolism in the Healthy and Diabetic Human Heart Using Hyperpolarized  $^{13}\text{C}$  MRI. *Circ. Res.* **2020**, 725–736.
- (3) Cunningham, C. H.; Lau, J. Y. C.; Chen, A. P.; Geraghty, B. J.; Perks, W. J.; Roifman, I.; Wright, G. A.; Connelly, K. A. Hyperpolarized  $^{13}\text{C}$  Metabolic MRI of the Human Heart: Initial Experience. *Circ. Res.* **2016**, 119 (11), 1177–1182.
- (4) Lewis, A. J. M.; Tyler, D. J.; Rider, O. Clinical Cardiovascular Applications of Hyperpolarized Magnetic Resonance. *Cardiovasc. Drugs Ther.* **2020**, 34 (2), 231–240.
- (5) Nelson, S. J.; Kurhanewicz, J.; Vigneron, D. B.; Larson, P. E. Z.; Harzstark, A. L.; Ferrone, M.; van Criekinge, M.; Chang, J. W.; Bok, R.; Park, I.; Reed, G.; Carvajal, L.; Small, E. J.; Munster, P.; Weinberg, V. K.; Ardenkjaer-Larsen, J. H.; Chen, A. P.; Hurd, R. E.; Odegardstuen, L.-I.; Robb, F. J.; Tropp, J.; Murray, J. A. Metabolic Imaging of Patients with Prostate Cancer Using Hyperpolarized  $[1\text{-}^{13}\text{C}]$ Pyruvate. *Sci. Transl. Med.* **2013**, 5 (198), 198ra108–198ra108.
- (6) Fiordelisi, M. F.; Cavaliere, C.; Auletta, L.; Basso, L.; Salvatore, M. Magnetic Resonance Imaging for Translational Research in Oncology. *J. Clin. Med.* **2019**, 8 (11), 1883.
- (7) Shukla-Dave, A.; Hricak, H. Role of MRI in Prostate Cancer Detection. *NMR Biomed.* **2014**, 27 (1), 16–24.
- (8) Gallagher, F. A.; Woitek, R.; McLean, M. A.; Gill, A. B.; Garcia, R. M.; Provenzano, E.; Riemer, F.; Kaggie, J.; Chhabra, A.; Ursprung, S.; Grist, J. T.; Daniels, C. J.; Zaccagna, F.; Laurent, M. C.; Locke, M.; Hilborne, S.; Frary, A.; Torheim, T.; Bournsnel, C.; Schiller, A.; Patterson, I.; Slough, R.; Carmo, B.; Kane, J.; Biggs, H.; Harrison, E.; Deen, S. S.; Patterson, A.; Lanz, T.; Kingsbury, Z.; Ross, M.; Basu, B.; Baird, R.; Lomas, D. J.; Sala, E.; Wason, J.; Rueda, O. M.; Chin, S. F.; Wilkinson, I. B.; Graves, M. J.; Abraham, J. E.; Gilbert, F. J.; Caldas, C.; Brindle, K. M. Imaging Breast Cancer Using Hyperpolarized Carbon-13 MRI. *Proc. Natl. Acad. Sci. U. S. A.* **2020**, 117 (4), 2092–2098.
- (9) Miloushev, V. Z.; Granlund, K. L.; Boltyskiy, R.; Lyashchenko, S. K.; DeAngelis, L. M.; Mellinghoff, I. K.; Brennan, C. W.; Tabar, V.; Yang, T. J.; Holodny, A. I.; Sosa, R. E.; Guo, Y. W.; Chen, A. P.; Tropp, J.; Robb, F.; Keshari, K. R. Metabolic Imaging of the Human Brain with Hyperpolarized  $^{13}\text{C}$  Pyruvate Demonstrates  $^{13}\text{C}$  Lactate Production in Brain Tumor Patients. *Cancer Res.* **2018**, 78 (14), 3755–3760.
- (10) Vaeggemose, M.; Schulte, R. F.; Laustsen, C. Comprehensive Literature Review of Hyperpolarized Carbon-13 Mri:

The Road to Clinical Application. *Metabolites* **2021**, *11* (4).

- (11) Ardenkjaer-Larsen, J. H.; Boebinger, G. S.; Comment, A.; Duckett, S.; Edison, A. S.; Engelke, F.; Griesinger, C.; Griffin, R. G.; Hilty, C.; Maeda, H.; Parigi, G.; Prisner, T.; Ravera, E.; Van Bentum, J.; Vega, S.; Webb, A.; Luchinat, C.; Schwalbe, H.; Frydman, L. Facing and Overcoming Sensitivity Challenges in Biomolecular NMR Spectroscopy. *Angew. Chemie - Int. Ed.* **2015**, *54* (32), 9162–9185.
- (12) Nikolaou, P.; Goodson, B. M.; Chekmenev, E. Y. NMR Hyperpolarization Techniques for Biomedicine. *Chem. - A Eur. J.* **2015**, *21* (8), 3156–3166.
- (13) Ardenkjaer-Larsen, J. H.; Fridlund, B.; Gram, A.; Hansson, G.; Hansson, L.; Lerche, M. H.; Servin, R.; Thaning, M.; Golman, K. Increase in Signal-to-Noise Ratio of > 10,000 Times in Liquid-State NMR. *Proc. Natl. Acad. Sci.* **2003**, *100* (18), 10158–10163.
- (14) Adams, R. W.; Aguilar, J. A.; Atkinson, K. D.; Cowley, M. J.; Elliott, P. I. P.; Duckett, S. B.; Green, G. R. R.; Khazal, I. G.; Lopez-Serrano, J.; Williamson, D. C. Reversible Interactions with Para-Hydrogen Enhance NMR Sensitivity by Polarization Transfer. *Science* (80-. ). **2009**, *323* (5922), 1708–1711.
- (15) Iali, W.; Roy, S. S.; Tickner, B. J.; Ahwal, F.; Kennerley, A. J.; Duckett, S. B. Hyperpolarising Pyruvate through Signal Amplification by Reversible Exchange (SABRE). *Angew. Chemie* **2019**, *131* (30), 10377–10381.
- (16) Tickner, B. J.; Semenova, O.; Iali, W.; Rayner, P. J.; Whitwood, A. C.; Duckett, S. B. Optimisation of Pyruvate Hyperpolarisation Using SABRE by Tuning the Active Magnetisation Transfer Catalyst. *Catal. Sci. Technol.* **2020**, *10* (5), 1343–1355.
- (17) Barskiy, D. A.; Knecht, S.; Yurkovskaya, A. V.; Ivanov, K. L. SABRE: Chemical Kinetics and Spin Dynamics of the Formation of Hyperpolarization. *Prog. Nucl. Magn. Reson. Spectrosc.* **2019**, *114–115*, 33–70.
- (18) Barskiy, D. A.; Shchepin, R. V.; Tanner, C. P. N.; Colell, J. F. P.; Goodson, B. M.; Theis, T.; Warren, W. S.; Chekmenev, E. Y. The Absence of Quadrupolar Nuclei Facilitates Efficient <sup>13</sup>C Hyperpolarization via Reversible Exchange with Parahydrogen. *ChemPhysChem* **2017**, *18* (12), 1493–1498.
- (19) Truong, M. L.; Theis, T.; Coffey, A. M.; Shchepin, R. V.; Waddell, K. W.; Shi, F.; Goodson, B. M.; Warren, W. S.; Chekmenev, E. Y. <sup>15</sup>N Hyperpolarization by Reversible Exchange Using SABRE-SHEATH. *J. Phys. Chem. C* **2015**, *119* (16), 8786–8797.
- (20) Theis, T.; Truong, M. L.; Coffey, A. M.; Shchepin, R. V.; Waddell, K. W.; Shi, F.; Goodson, B. M.; Warren, W. S.; Chekmenev, E. Y. Microtesla SABRE Enables 10% Nitrogen-15 Nuclear Spin Polarization. *Journal of the American Chemical Society.* **2015**, pp 1404–1407.
- (21) Knecht, S.; Blanchard, J. W.; Barskiy, D.; Cavallari, E.; Dagys, L.; van Dyke, E.; Tsukanov, M.; Bliemel, B.; Münnemann, K.; Aime, S.; Reineri, F.; Levitt, M. H.; Buntkowsky, G.; Pines, A.; Blümler, P.; Budker, D.; Eills, J. Rapid Hyperpolarization and Purification of the Metabolite Fumarate in Aqueous Solution. *Proc. Natl. Acad. Sci. U. S. A.* **2021**, *118* (13), 1–6.
- (22) Kovtunov, K. V.; Pokochueva, E. V.; Salnikov, O. G.; Cousin, S. F.; Kurzbach, D.; Vuichoud, B.; Jannin, S.; Chekmenev, E. Y.; Goodson, B. M.; Barskiy, D. A.; Koptuyug, I. V. Hyperpolarized NMR Spectroscopy: D-DNP, PHIP, and SABRE Techniques. *Chem. - An Asian J.* **2018**, *13* (15), 1857–1871.
- (23) Cavallari, E.; Carrera, C.; Sorge, M.; Bonne, G.; Muchir, A.; Aime, S.; Reineri, F. The <sup>13</sup>C Hyperpolarized Pyruvate Generated by ParaHydrogen Detects the Response of the Heart to Altered Metabolism in Real Time. *Sci. Rep.* **2018**, *8* (1), 8366.
- (24) Eills, J.; Cavallari, E.; Carrera, C.; Budker, D.; Aime, S.; Reineri, F. Real-Time Nuclear Magnetic Resonance Detection of Fumarase Activity Using Parahydrogen-Hyperpolarized [1- <sup>13</sup>C]Fumarate. *J. Am. Chem. Soc.* **2019**, *141* (51), 20209–20214.
- (25) Ripka, B.; Eills, J.; Kouřilová, H.; Leutzsch, M.; Levitt, M. H.; Münnemann, K. Hyperpolarized Fumarate via Parahydrogen. *Chem. Commun.* **2018**, *54* (86), 12246–12249.
- (26) Knecht, S.; Blanchard, J. W.; Barskiy, D.; Cavallari, E.; Dagys, L.; Dyke, E. Van. Rapid Hyperpolarization and Purification of the Metabolite Fumarate in Aqueous Solution. *ChemRxiv* **2020**, No. 1.
- (27) Cavallari, E.; Carrera, C.; Aime, S.; Reineri, F. <sup>13</sup>C MR Hyperpolarization of Lactate by Using ParaHydrogen and Metabolic Transformation in Vitro. *Chem. - A Eur. J.* **2017**, *23* (5), 1200–1204.
- (28) Cavallari, E.; Carrera, C.; Aime, S.; Reineri, F. Studies to Enhance the Hyperpolarization Level in PHIP-SAH-Produced C13-Pyruvate. *J. Magn. Reson.* **2018**, *289*, 12–17.
- (29) Chapman, B.; Joalland, B.; Meersman, C.; Etedgui, J.; Swenson, R. E.; Krishna, M. C.; Nikolaou, P.; Kovtunov, K. V.; Salnikov, O. G.; Koptuyug, I. V.; Gemeinhardt, M. E.; Goodson, B. M.; Shchepin, R. V.; Chekmenev, E. Y. Low-Cost High-Pressure Clinical-Scale 50% Parahydrogen Generator Using Liquid Nitrogen at 77 K. *Anal. Chem.* **2021**, *93* (24), 8476–8483.
- (30) TomHon, P.; Akeroyd, E.; Lehmkuhl, S.; Chekmenev, E. Y.; Theis, T. Automated Pneumatic Shuttle for Magnetic Field Cycling and Parahydrogen Hyperpolarized Multidimensional NMR. *J. Magn. Reson.* **2020**, *312*, 106700.
- (31) Theis, T.; Truong, M. L.; Coffey, A. M.; Shchepin, R. V.; Waddell, K. W.; Shi, F.; Goodson, B. M.; Warren, W. S.; Chekmenev, E. Y. Microtesla SABRE Enables 10% Nitrogen-15 Nuclear Spin Polarization. *J. Am. Chem. Soc.* **2015**, *137* (4), 1404–1407.
- (32) Colell, J. F. P.; Logan, A. W. J.; Zhou, Z.; Shchepin, R. V.; Barskiy, D. A.; Ortiz, G. X.; Wang, Q.; Malcolmson, S. J.; Chekmenev, E. Y.; Warren, W. S.; Theis, T. Generalizing, Extending, and Maximizing Nitrogen-15 Hyperpolarization Induced by Parahydrogen in Reversible Exchange. *J. Phys. Chem. C* **2017**, *121* (12), 6626–6634.
- (33) MacCulloch, K.; Tomhon, P.; Browning, A.; Akeroyd, E.; Lehmkuhl, S.; Chekmenev, E. Y.; Theis, T. Hyperpolarization of Common Antifungal Agents with SABRE. *Magn. Reson. Chem.* **2021**, No. June, 1–11.
- (34) Kiryutin, A. S.; Yurkovskaya, A. V.; Ivanov, K. L. <sup>15</sup>N SABRE Hyperpolarization of Metronidazole at Natural Isotope Abundance. *ChemPhysChem* **2021**, 1–9.
- (35) Hermkens, N. K. J.; Feiters, M. C.; Rutjes, F. P. J. T.; Wijmenga, S. S.; Tessari, M. High Field Hyperpolarization-EXSY Experiment for Fast Determination of Dissociation Rates in SABRE Complexes. *J. Magn. Reson.* **2017**, *276* (2017), 122–127.
- (36) Kidd, B. E.; Gesiorski, J. L.; Gemeinhardt, M. E.; Shchepin, R. V.; Kovtunov, K. V.; Koptuyug, I. V.; Chekmenev, E. Y.; Goodson, B. M. Facile Removal of Homogeneous SABRE Catalysts for Purifying Hyperpolarized Metronidazole, a Potential Hypoxia Sensor. *J. Phys. Chem. C* **2018**, *122* (29), 16848–16852.
- (37) Iali, W.; Olaru, A. M.; Green, G. G. R.; Duckett, S. B. Achieving High Levels of NMR-Hyperpolarization in Aqueous Media With Minimal Catalyst Contamination Using SABRE. *Chem. - A Eur. J.* **2017**, *23* (44), 10491–10495.